Accretion-induced Collapse of Dark Matter-admixed Rotating White Dwarfs: Dynamics and Gravitational-wave Signals

Ho-Sang Chan [ID],[1] Ming-chung Chu [ID],[1] Shing-Chi Leung [ID],[2, 3] and Lap-Ming Lin [ID][1]

[1]*Department of Physics and Institute of Theoretical Physics, The Chinese University of Hong Kong, Shatin, N.T., Hong Kong S.A.R., China*
[2]*Department of Mathematics and Physics, SUNY Polytechnic Institute, 100 Seymour Road, Utica, New York 13502, USA*
[3]*TAPIR, Walter Burke Institute for Theoretical Physics, Mailcode 350-17, Caltech, Pasadena, CA 91125, USA*

ABSTRACT

We present two-dimensional hydrodynamic simulations of the accretion-induced collapse (AIC) of rotating white dwarfs admixed with an extended component of dark matter (DM) comprising of sub-GeV degenerate fermionic DM particles. We find that the DM component would follow the collapse of the normal matter (NM) component to become a bound DM core, with a time scale comparable to that of the NM. Thus, our simulations demonstrate how a DM-admixed neutron star could form through DM-admixed AIC (DMAIC) for the first time. The gravitational-wave (GW) signature from the DMAIC shows distinctive features. In the diffusive DM limit, the admixture of DM indirectly suppresses the post-bounce spectral peak of the NM GWs; In the compact DM limit, the collapse dynamics of the DM in a Milky Way event generate GWs that are strong enough to be detectable by Advanced LIGO as continuous low-frequency (< 1000 Hz) signals after the NM core bounce. We further discover a relationship between the DM mass and its GW peak frequency, and we provide an empirical formula that fits the relation. Not only is our study the first-ever computation of GW from a collapsing DM, but these findings also provide the key features to identify DM in AIC events through future GW detections.

Keywords: Dark matter(353), White dwarf stars(1799), Stellar rotation(1629), Gravitational waves(678), Neutron stars(1108)

1. INTRODUCTION

1.1. *Dark Matter-admixed Astrophysical Objects*

It is widely believed that dark matter (DM) constitutes the major mass-energy component of galaxy clusters (**?**) and large-scale structures of the Universe (Davis et al. 1985). Besides terrestrial experiments, physicists are tackling the DM problem through astrophysical observations. It is shown that in a region with a high concentration of DM particles, DM could be captured by normal matter (NM, Sulistiyowati et al. 2014; Arun et al. 2019). Therefore, it is natural to expect stellar objects composed of NM and DM. There have been extensive theoretical studies on the possible effects of the DM admixture on the stellar evolution (Lopes & Lopes 2019; Clea et al. 2020; Raen et al. 2021). Unusual stellar objects consistent with these models might hint at the existence of DM-admixed stars. Furthermore, there are studies utilizing DM-admixed star models to understand the properties of DM. For instance, Leung et al. (2022) proposed a method for inferring the DM particle mass by measuring the tidal deformability of neutron stars. Using the DM-admixed neutron star model, Bramante et al. (2013) and Bell et al. (2013) gave constraints on the bosonic DM particle mass and annihilation cross section. These examples show that DM-admixed stellar objects could be a promising channel to probe astrophysical DM.

1.2. *Rotating White Dwarfs*

The majority of studies on white dwarfs (WD) assumed they are not rotating, but observational evidences showed the opposite (Spruit 1998; Kawaler 2004). It was suggested that WDs gain angular momentum through accretion from a companion star (Langer et al. 2003; Yoon & Langer 2004) or mergers between two or more WDs (Gvaramadze et al. 2019; Pshirkov et al. 2020). Therefore, rotation is an important ingredient of the full

picture of WD structure and evolution (Yoon & Langer 2004; Yoon, S.-C. & Langer, N. 2005). In addition, rotating WDs have been proposed to be progenitors of super-luminous thermonuclear supernovae because rotating WDs could support more mass than their traditional Chandrasekhar limit (Pfannes, J. M. M. et al. 2010; Wang et al. 2014; Fink, M. et al. 2018). Recently, theoretical studies have been made on finite-temperature corrections to the modeling of rotating WDs (Boshkayev 2018; Yoshida 2019), as well as effects of the strong magnetic field on the equilibrium structures of WDs (Franzon & Schramm 2015; Bera & Bhattacharya 2016; Chatterjee et al. 2017), for which the WD rotation takes a critical role.

1.3. *Accretion-induced Collapse*

It was widely believed that a WD would undergo a thermouclear explosion when its mass is approaching the canonical Chandrasekhar limit. However, if the WD contains an Oxygen-Neon core, Accretion-Induced Collapse (AIC) is possible as its mass increases towards the Chandrasekhar limit through stable accretion from a companion object (Nomoto & Kondo 1991; Wang 2018; Ruiter et al. 2019), though a binary WD merger seems to be another possible scenario (Liu & Wang 2020). The collapse is triggered by electron capture in the degenerate matter, weakening the electron degenerate pressure (Brooks et al. 2017). On the other hand, pycnonuclear burning is also possible in such an extremely dense core. Hence the ultimate fate of an Oxygen-Neon WD would depend on the competition between nuclear runaway and electron capture (Wang & Liu 2020). However, it was later found that the central temperature of Oxygen-Neon WDs is insufficient for explosive oxygen-neon burning (Wu & Wang 2018). Even if deflagration occurs, it fails to unbind the WD, which directly leads to a collapse for a wide range of parameters (Leung & Nomoto 2019; Zha et al. 2019b; Leung et al. 2020).

Besides the iron-core collapse of massive stars, the AIC of WDs has been proposed as another channel for forming neutron stars. However, AIC is much less luminous than typical core-collapse supernovae. The small amount of nickel synthesized indicates that AICs are usually faint transients (Darbha et al. 2010). On the other hand, AIC emits radio signatures (Moriya 2016) and has been hypothesized as a source candidate for Fast Radio Burst (Margalit et al. 2019) and Millisecond Pulsars (Wang et al. 2022). Electromagnetic-wave detection of AIC would be a challenging but possible task. One possible way to search for AIC is by neutrino detection because a neutrino burst should accompany AIC after the WD dynamical collapse (Dar et al. 1992). The burst luminosity could be as large as 10^{55} erg s^{-1} (Zha 2019, Dessart et al. 2006). On the other hand, the collapse dynamics of the compact iron core are expected to produce strong GW signals (Ott et al. 2005; Ott 2009). Hence, searching for AIC would rely on future GW detection. There have been some efforts to predict the GW signature from an AIC. Dessart et al. (2006) simulated 2D AIC with neutrino transport and estimated the GW emission from AIC via the Newtonian quadruple formalism. They concluded that Milky Way AIC events could be detected by LIGO-class detectors. Abdikamalov et al. (2010) found that the GW signals from an AIC show a generic "Type III" shape, though detailed neutrino physics has been omitted.

1.4. *Motivations*

Although DM-admixed neutron stars have been studied and applied to explain anomalous compact objects, there is still no in-depth research on their formation channel. Even though Leung et al. (2019); Zha et al. (2019a) numerically investigated DMAIC, they assumed the DM component to be spherically symmetric and non-moving. As pointed out by Leung et al. (2019), the non-movable DM approximation may break down if the dynamical time scales for DM and NM become comparable, and the dynamical modeling of the DM becomes important. They also pointed out that there is a moment during the collapse in which the NM has a mass density comparable with that of the DM. Also, Chan et al. (2021) showed that fermionic DM with a sub-GeV particle mass would produce a massive and extended component comparable in size to that of the NM. In such a scenario, modeling the DM dynamics would be necessary. In this study, we extend the multidimensional simulations by Zha et al. (2019a) to include also the DM dynamical evolution. Our study aims to investigate if DMAIC could make a DM-admixed neutron star when the DM motion is taken into account and to predict the corresponding GW signature to facilitate searching for DM through observing AIC in the future. The structure of the paper is as follows: we present the methodology in Section 2. We then present our simulation results in Section 3. Finally, we conclude our study in Section 4.

2. METHODOLOGY

2.1. *Equation of Hydrostatic Equilibrium*

We compute DM-admixed rotating WDs (DMRWDs) as DM-admixed AIC (DMAIC) progenitors by solving the Newtonian hydrostatic equations, including the cen-

tripetal force:

$$\vec{\nabla}P_1 = -\rho_1\vec{\nabla}\Phi,$$
$$\vec{\nabla}P_2 = -\rho_2\vec{\nabla}\Phi + [\rho_2\omega_2(s)^2 s]\hat{s}, \tag{1}$$
$$\nabla^2\Phi = 4\pi G(\rho_1 + \rho_2).$$

Here, the subscript $i = 1(2)$ denotes the DM (NM) quantities, and ρ, P, ω, and Φ are the density, pressure, angular speed, and gravitational potential of the fluid element. s is the perpendicular distance from the rotation axis, and $\hat{s}$ is the unit vector orthogonal to and pointing away from that axis. The angular speed is assumed to be a function of s only. We consider Newtonian framework because the rotation speed and compactness of WDs are low.

We follow Eriguchi & Mueller (1985), Hachisu (1986) and Aksenov & Blinnikov (1994) to integrate the equations of equilibrium:

$$H_i + \Phi + \delta_{i2}h_i^2\psi_i = C_i,$$
$$\int \frac{dP_i}{\rho_i} = H_i, \tag{2}$$
$$\int \omega(s)_i^2 s\,ds = -h_i^2\psi_i,$$

where C_i is an integration constant, H is the enthalpy, ψ is the rotational potential, and h^2 is a constant to be determined Hachisu (1986). We solve the equilibrium equations for the DM and NM using a two-fluid, self-consistent field method (Chan et al. 2022, submitted).

2.2. Rotation Rules

We have considered rotation profiles for the NM from Hachisu (1986) and Yoshida (2019) including (1) the rigid rotation:

$$\omega(s)_2^2 = \Omega_2^2, \tag{3}$$

and (2) the "Kepler" profile:

$$\omega(s)_2^2 \propto 1/(d^{3/2} + s^{3/2})^2, \tag{4}$$

whiich resembles a rapidly rotating core surrounded by an envelope rotating at its Keplerian limit. Here, d is the rotating core radius.

We integrate the angular velocity to obtain the effective potential of the rigid rotation:

$$\psi_2 = s^2/2. \tag{5}$$

The effective potential for the Kepler rule is:

$$\psi_2 = -\frac{1}{9}\left[-\frac{6\sqrt{s}}{s^{\frac{3}{2}} + d^{\frac{3}{2}}} + \frac{1}{d}\ln\left(\frac{(\sqrt{d} + \sqrt{s})^2}{d + s - \sqrt{sd}}\right)\right.$$
$$\left. - \frac{2\sqrt{3}}{d}\tan^{-1}\left(\frac{1 - 2\sqrt{s/d}}{\sqrt{3}}\right)\right]. \tag{6}$$

2.3. Hydrodynamic Evolution

To simulate DMAIC, we solve the two-dimensional Euler equations assuming axial symmetry:

$$\partial_t\rho_i + \nabla\cdot(\alpha\rho_i\vec{v_i}) = 0,$$
$$\partial_t(\rho_i\vec{v_i}) + \nabla\cdot[\alpha\rho_i(\vec{v_i}\otimes\vec{v_i})] + \nabla(\alpha P_i) =$$
$$-\alpha(\rho_i - P_i)\nabla\Phi. \tag{7}$$

Here, $\alpha = \exp(-\phi/c^2)$ is the lapse function with c being the speed of light. It is used to mimic general relativistic time-dilation effects and has been applied to study the first-order quantum chromodynamics phase transition in core-collapse supernovae (Zha et al. 2020). We also solve the advection equation for the NM total internal energy density $\tau_2 = \rho_2\epsilon_2 + \rho_2 v_2^2/2$ and electron fraction Y_e:

$$\partial_t\tau_2 + \nabla\cdot[\alpha(\tau_2 + P_2)\vec{v_2}] = -\alpha\rho_2\vec{v_2}\cdot\nabla\Phi,$$
$$\partial_t(\rho_2 Y_e) + \nabla\cdot(\alpha\rho_2 Y_e\vec{v_2}) = 0. \tag{8}$$

The gravitational potential Φ is solved by a multipole solver, for which we adopt the one by Couch et al. (2013) that can reduce error due to computing the potential at the cell center while using the mass density at that point. To mimic general relativistic strong-field effects, we use the modified case A potential (Müller et al. 2008) as an additional correction to the Newtonian potential:

$$\Phi \to \Phi - \langle\Phi\rangle + \Phi_{\rm TOV,1} + \Phi_{\rm TOV,2},$$
$$\langle\Phi\rangle = -4\pi\int_0^\infty dr' r'^2\frac{\langle\rho_1 + \rho_2\rangle}{|r - r'|}. \tag{9}$$

Here, r is the radial distance and $\langle\rho_1 + \rho_2\rangle$ represents the angular average of the total density. $\Phi_{\rm TOV,i}$ for $i =$1, 2 are the relativistic corrections:

$$\Phi_{\rm TOV,i} = -4\pi\int_0^\infty \frac{dr'}{r'^2}\frac{1}{\Gamma_i^2}\left(\frac{m_{\rm TOV,i}}{4\pi} + r'^3 P_i\right)$$
$$\left(1 + \epsilon_i + \frac{P_i}{\rho_i}\right),$$
$$m_{\rm TOV,i} = 4\pi\int_0^r dr' r'^2\Gamma_i\rho_i(1 + \epsilon_i), \tag{10}$$
$$\Gamma_i = \sqrt{1 + v_{r,i}^2 - \frac{2m_{\rm TOV,i}}{r}},$$

where $v_{r,i}$ is the radial velocity. We adopt a finite-volume approach to solve the hydrodynamic equation in spherical coordinates (Mignone 2014). We use the piecewise parabolic method (Colella & Woodward 1984) to reconstruct primitive variables at the cell interface, and the HLLE Riemann solver (Toro 2009) to compute fluxes across cell boundaries. The reconstruction and flux evaluation are done on a dimension-by-dimension basis. We discretize the temporal evolution using the method of

lines where the strong stability-preserving 5-step, 4th-order Runge-Kutta method is implemented (Gottlieb et al. 2011). In addition to the (modified) Euler equation, we also append the internal energy equation for the NM:

$$\partial_t(\rho_2\epsilon_2) + \nabla \cdot \{\alpha[(\rho_2\epsilon_2) + P_2]\vec{v_2}\} = \\ \vec{v_2} \cdot \nabla(\alpha P_2) - \alpha P_2(\vec{v_2} \cdot \nabla\Phi). \quad (11)$$

And it not only allows one to interpolate internal energy density ϵ to the cell interface directly so that computational cost due to evaluating ϵ at the cell interface could be reduced, but it also reduces the error of ϵ due to advection (Zingale et al. 2020). We adopt a computational grid similar to Skinner et al. (2016), in which the analytic function describes the position of the radial cell interface as:

$$r = A_t \sinh(x_t i / A_t). \quad (12)$$

Here, i is the cell index. We set $x_t = 0.5$ and $A_t = 150$ so that a central resolution of around 0.34 km is provided, while a total of 500 computational grid is used to contain the progenitor. We set the angular resolution to be 20, which we find to be sufficient for ensuring convergence in GW signals for both the NM and DM.

2.4. Micro-physics

After mapping the density profiles of the NM and DM components computed from Section 2.1, we assign a initial temperature profile to the NM (Dessart et al. 2006):

$$T(\rho) = T_c(\rho/\rho_c)^{0.35}. \quad (13)$$

Here, $T_c = 10^{10}$ K is the central temperature and $\rho_c = 5 \times 10^{10}$ gcm^{-3} is the central density. The AIC is initiated by the core electron capture process. We implement the parameterized electron capture scheme described in Liebendorfer (2005) to simulate such process. In their work, Y_e depends on ρ_2 as:

$$x(\rho_2) = \max\left[-1, \min\left(1, \frac{2 - \log\rho_2 - \log\rho_\alpha - \log\rho_\beta}{\log\rho_\alpha - \log\rho_\beta}\right)\right],$$
$$Y_e(x) = \frac{1}{2}(Y_b + Y_a) + \frac{x}{2}(Y_b - Y_a) + \\ Y_c[1 - |x| + 4|x|(|x| - 1/2)(|x| - 1)]. \quad (14)$$

Here, $\log\rho_\alpha$, $\log\rho_\beta$, Y_a, Y_b, and Y_c are fitting parameters and are obtained by Leung et al. (2019) and Zha et al. (2019a). We first assign an initial equilibrium Y_e profile to the NM using Equation 14. We then start the electron capture process by updating Y_e at each time step using the same equation. We force Y_e to be strictly decreasing with time. We terminate the electron capture process

once the core bounce condition (Liebendorfer 2005) is achieved, which is defined to be the core NM entropy larger than $3k_B$, where k_B is the Boltzman constant.

2.5. Gravitational-wave Signals

We use the quadrupole formula in the weak-field approximation to compute the GW strain (Finn & Evans 1990; Moenchmeyer et al. 1991):

$$h_+ = \frac{3}{2}\frac{G}{Dc^4}\sin^2\theta\frac{d^2}{dt^2}I_{zz}. \quad (15)$$

Here, $D = 10$ kpc is the distance, and θ is the orientation to the collapsing DMRWD. I_{zz} is the moment of inertia tensor:

$$I_{zz} = \frac{1}{3}\int_{\text{All Space}}(\rho_1 + \rho_2)r^2 P_2(\cos\theta)d\tau. \quad (16)$$

2.6. Equations of State

To simulate AICs, we first use the ideal degenerate Fermi gas EOS for equilibrium structure construction. Following the subsequent collapse dynamics, we use the nuclear matter EOS given by Shen et al. (2011), widely used in simulating core-collapse supernovae and neutron star dynamics. We adopt the ideal degenerate Fermi gas EOS for the DM component (Narain et al. 2006).

3. RESULTS AND DISCUSSION

We define $\bar{t}$ as the time after the NM core bounce, and we terminate all our simulations at $\bar{t} = 0.1$ s.

3.1. The Diffusive Dark Matter Limit

We have computed a series of DMRWD models as DMAIC progenitors. The stellar parameters of these progenitors have been listed in Table 1 for reference. The progenitors have increasing DM mass fractions ϵ_{DM} from 0.01 to 0.2. The progenitors include rigidly-rotating and differentially-rotating DMRWDs with different d as described in Equation 4. In particular, d is chosen so that $\rho_2(r = d, \theta = \frac{\pi}{2}) = \alpha_d\rho_{2c}$. We choose $\alpha_d = 0.1$ and 0.01. Another free parameter to be specified for these progenitors is the central angular velocity Ω_c. We adjust this value for rigidly-rotating DMRWDs so that the corresponding pure NM progenitor almost rotates at the Keplerian limit and that a total mass of $\approx 1.8\ M_\odot$ is achieved for a pure NM, differentially rotating WD. We fix the DM particle mass to be 0.1 GeV for all of these progenitors. As shown in Chan et al. (2021), the fluid component formed by DM particles with such a mass will be more diffusive and comparable in size to that of the NM.

Table 1. The stellar parameters for different DMAIC progenitors. They include rigid (labelled Rigid) and differentially (labelled Kepler) rotating DMRWDs. All progenitors have NM central density of 5×10^{10} gcm^{-3}. The DM particle mass is 0.1 GeV.

Model	M_{NM}	M_{DM}	α_d	$\log_{10}\rho_{1c}$	Ω_c	R_{eNM}	R_{eDM}	ϵ_{DM}	t_b	$\log_{10}\rho_{1b}$	$\log_{10}\rho_{2b}$	M_{PNS}
-	$(M_\odot)$	$(M_\odot)$	-	(gcm^{-3})	(s^{-1})	(km)	(km)	-	(ms)	(gcm^{-3})	(gcm^{-3})	$(M_\odot)$
Rigid-NM	1.477	0.000	-	-	10.8	1105	-	0	53.151	-	14.318	1.217
Rigid-0.01	1.447	0.015	-	8.816	10.8	1098	400	0.01	53.424	11.078	14.317	1.194
Rigid-0.03	1.416	0.044	-	8.980	10.8	1027	568	0.03	53.717	11.093	14.315	1.170
Rigid-0.05	1.397	0.074	-	9.046	10.8	980	695	0.05	53.902	11.097	14.316	1.157
Rigid-0.07	1.384	0.104	-	9.086	10.8	948	807	0.07	54.035	11.100	14.315	1.146
Rigid-0.09	1.374	0.136	-	9.114	10.8	923	904	0.09	54.139	11.102	14.315	1.139
Rigid-0.1	1.307	0.152	-	9.125	10.8	910	954	0.1	54.183	11.103	14.315	1.136
Rigid-0.2	1.343	0.336	-	9.193	10.8	857	1379	0.2	54.496	11.107	14.313	1.119
Kepler-NM-d001	1.770	0.000	0.01	-	32.5	1826	-	0	35.124	-	14.355	1.597
Kepler-0.01-d001	1.725	0.017	0.01	8.853	32.5	1766	420	0.01	35.352	11.073	14.352	1.553
Kepler-0.03-d001	1.662	0.051	0.01	9.016	32.5	1494	587	0.03	35.647	11.086	14.351	1.498
Kepler-0.05-d001	1.623	0.085	0.01	9.082	32.5	1343	710	0.05	35.835	11.091	14.352	1.463
Kepler-0.07-d001	1.596	0.120	0.01	9.122	32.5	1256	812	0.07	35.969	11.094	14.350	1.439
Kepler-0.09-d001	1.577	0.156	0.01	9.150	32.5	1190	904	0.09	36.072	11.096	14.350	1.419
Kepler-0.1-d001	1.569	0.174	0.01	9.162	32.5	1159	948	0.1	36.116	11.097	14.350	1.411
Kepler-0.2-d001	1.518	0.379	0.01	9.232	32.5	1020	1352	0.2	36.424	11.101	14.349	1.362
Kepler-NM-d001	1.771	0.000	0.1	-	45.2	1106	-	0	32.311	-	14.354	1.598
Kepler-0.01-d01	1.727	0.017	0.1	8.860	45.2	1098	417	0.01	32.555	11.070	14.353	1.555
Kepler-0.03-d01	1.677	0.052	0.1	9.026	45.2	1062	579	0.03	32.788	11.084	14.354	1.511
Kepler-0.05-d01	1.647	0.087	0.1	9.094	45.2	1034	700	0.05	32.924	11.088	14.351	1.483
Kepler-0.07-d01	1.625	0.122	0.1	9.135	45.2	1007	801	0.07	32.024	11.092	14.351	1.460
Kepler-0.09-d01	1.609	0.159	0.1	9.164	45.2	987	892	0.09	33.101	11.095	14.352	1.446
Kepler-0.1-d01	1.602	0.178	0.1	9.176	45.2	980	941	0.1	33.133	11.096	14.352	1.439
Kepler-0.2-d01	1.556	0.389	0.1	9.247	45.2	916	1343	0.2	33.364	11.101	14.355	1.396

NOTE—In this table, R_{eNM} (R_{eDM}) is the equatorial radius of the progenitors for the NM (DM) component. ρ_{1c} is the DM central density, ϵ_{DM} is the DM fraction, and t_b is the bounce time. ρ_{2b} (ρ_{1b}) is the maximum NM (DM) density at core bounce. M_{PNS} is the proto-neutron star mass, defined as summing all the NM mass with $\rho_2 > 10^{11}$ gcm^{-3} at the end of the simulations.

3.1.1. *The Collapse Dynamics*

We first focus on the collapse dynamics of DMAIC. From Table 1, we observe that the admixture of DM delays the time of core bounce and reduce the proto-neutron star mass, which is similar to the results by Leung et al. (2019) and Zha et al. (2019a). We show the maximum NM density evolution for the rigidly-rotating DMAIC models in the right-hand panel of Figure 1. Despite having different initial and proto-neutron star masses (c.f. Table 1), the maximum NM density evolution is almost identical for all DMAIC models. The final maximum NM densities are also insensitive to the DM mass fraction ϵ_{DM}. Furthermore, we find that AIC is successful for all DMAIC progenitors. This is in con-trast to the results presented by Leung et al. (2019) and Zha et al. (2019a), where the disagreement between our results and theirs is because we are assuming different DM particle masses. Their work assumed a heavy (1 GeV) DM particle mass, leading to a more compact DM core with a large central density. Thus, it significantly impacts the NM density profile near its centre. The NM density decreases sharply due to the strong gravitational force provided by the compact DM core. Electron capture is less efficient, so the NM component's effective adiabatic index remains near $\frac{4}{3}$. We assumed a light (0.1 GeV) DM particle mass in our study. The DM component is more diffusive and extended. Hence it brings a less significant impact to the NM density profile near its core. We demonstrate the NM density
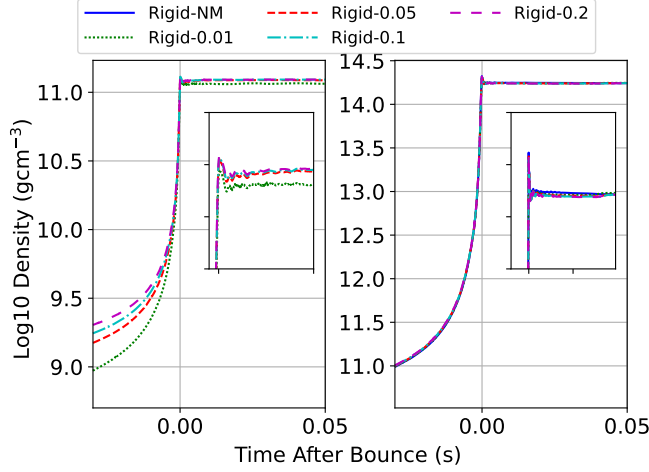
Figure 1. Evolution of the maximum density the rigidly-rotating DMAIC models. The left- (right-) hand panel is for the DM (NM) component. Since there are only minimal deviations among different DM-admixed models, we show a magnified density evolution plot in each panel.
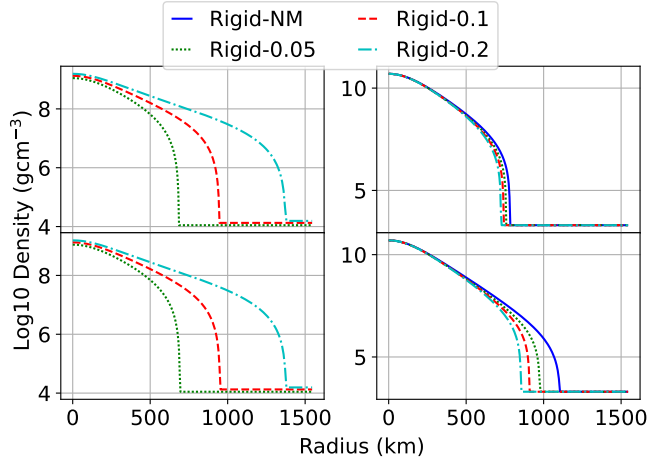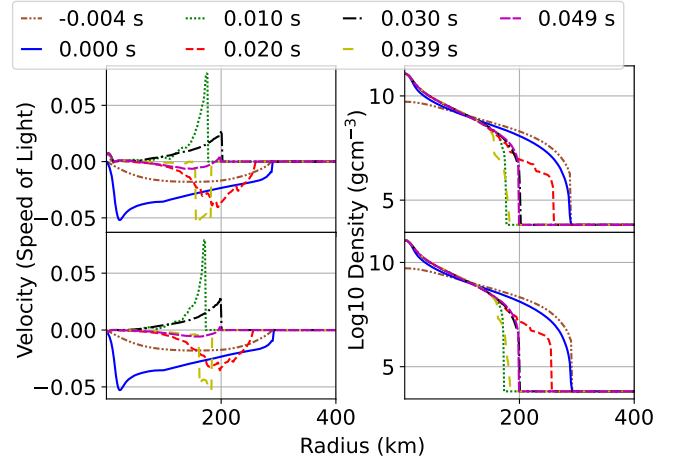

Figure 3. Evolution of the DM radial density and velocity profile evolution of the Rigid-0.01 DMAIC model. The left- (right-) hand panel is for the velocity (density). The upper (lower) sub-panel in each panel is for the polar (equatorial) profiles.

Figure 2. Initial density profiles for the rigidly-rotating DMAIC progenitors. The left- (right-) hand panel is for the DM (NM) component. The upper (lower) sub-panel in each panel is for the polar (equatorial) density profiles.
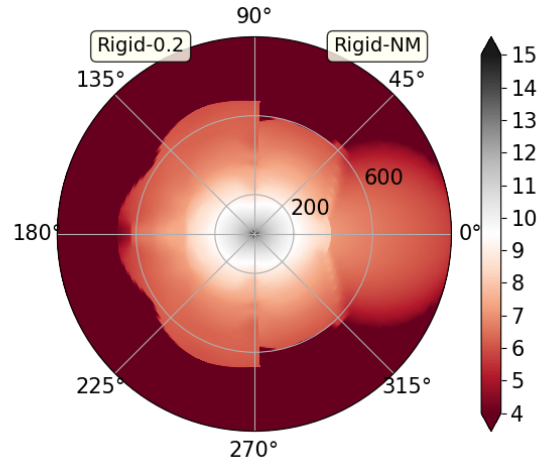
Figure 4. NM density contour plot for two different rigidly-rotating DMAIC models at the end of the simulations. The right- (left-) hand plot is for the Rigid-NM (Rigid-0.2) model. Densities are in the $\log_{10}$ scale of $\mathrm{gcm^{-3}}$. The radial distance is in km.

profile changes with increasing DM mass fraction ϵ_{DM} in the right-hand panel of Figure 2. We observe that when more DM is admixed, the changes in the NM density profile are primarily at the outer envelope. The core of the NM component remains almost unchanged. The collapse dynamics of a WD are governed by the dense core, where ρ_2 is large enough to initiate electron capture. Since the core NM density profile changes are insensitive to the DM mass fraction ϵ_{DM} in our study, it is natural to expect generic collapse dynamics for all rigidly-rotating DMRWDs.

We discovered that the DM component collapses with the NM component to form a bound DM core. We show the DM density profile evolution in the left-hand panel of Figure 3. The DM density evolves similarly to the NM densitiy, but the DM density remains stable after the NM core bounce. We show the density profile evolution for a particular model Rigid-0.01 in the right-hand panel of Figure 3 as an example. The DM radius contracts from ~ 350 km at $\bar{t} = 0.014$ s, to ~ 180 km at $\bar{t} = 0.01$ s. Although the DM radius increases at $\bar{t} = 0.02$ s, the DM component gradually contracts to

~ 200 km at $\bar{t} = 0.03$ s and pulsates around $\sim 180-200$ km. And this suggests that a bound DM component has formed with negligible mass loss. We show the DM velocity profile evolution of the same DMRWD model in the left-hand panel of Figure 3. The post-bounce velocity shock breaks through the DM surface around $\bar{t} = 0.01$ s. However, the shock is too weak to unbind the DM component. The strength of the shock gradually reduces and becomes a sound wave that propagates inside the DM component. This also explains the pulsation of the DM component between $\bar{t} = 0.03$ and 0.049 s.

3.1.2. The Formation of DM-admixed Neutron Stars

What are the astrophysical implications of our findings? DM-admixed neutron stars have been extensively studied in the past decade. For instance, Bhat & Paul (2020) showed that the admixture of DM can explain the cooling rate of some pulsars/neutron stars, e.g., PSR B0656+14, PSR B1706-44 and PSR B2334+61, which could not be explained if the popular APR equation of state (EOS) is assumed. Das et al. (2021) and Lee et al. (2021) discuss the anomalous 2.6 $M_\odot$ object from the gravitational-wave event GW190814 (Abbott et al. 2020) as a possible DM-admixed neutron star. However, the formation channel of DM-admixed neutron stars has never been addressed in depth. Although Zha et al. (2019b) performed DMAIC simulations, their work relies on the assumption that the DM is compact and non-movable. Our self-consistent, two-fluid simulations show that the AIC of a DMRWD would produce a DM-admixed (rotating) neutron star, such that the DM component is gravitationally bound with negligible mass loss. The collapse of DM also happens with a time scale similar to that of NM. Therefore, we have shown numerically that it is possible to form a DM-admixed neutron star through DMAIC.

3.1.3. Gravitational-wave Signatures

The non-luminous nature of the DM makes it difficult to be detected through conventional telescopes. The weak electromagnetic signatures from a typical AIC also hinder indirect DM detection by comparing AIC luminosities. Therefore, we rely on predicting the GW signatures generated by both the NM and DM components.

Equation 14 suggests that the moment of inertia tensor I_{zz} is separable into individual DM and NM components:

$$I_{zz} = I_{zz,1} + I_{zz,2},$$
$$I_{zz,i} = \frac{1}{3} \int_{\text{All Space}} \rho_i r^2 P_2(\cos\theta) d\tau. \quad (17)$$
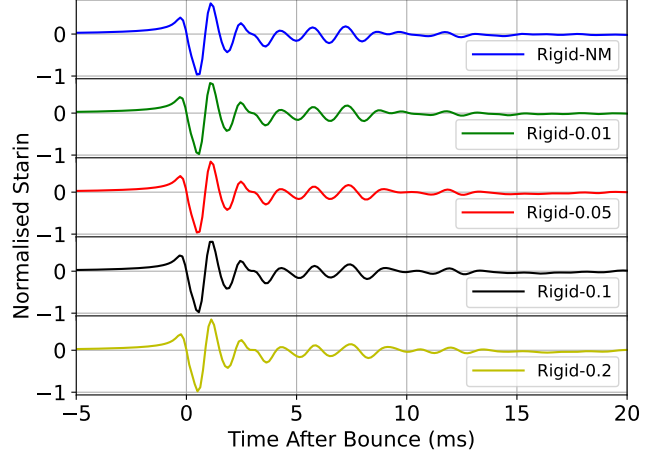

Figure 5. Total GW strains for the rigidly-rotating DMAIC models. We normalised all the GW strains to the corresponding maximum amplitude of the Rigid-NM model. The normalisation constant is 7.53×10^{-21}.
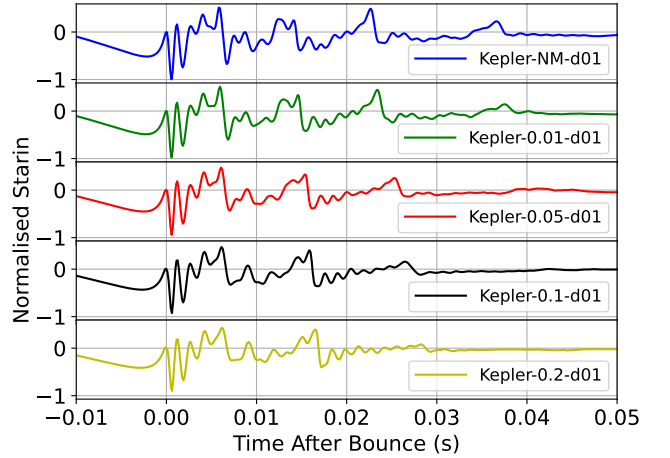

Figure 6. Same as Figure 5, but for the Kepler-rotating and $\alpha_d = 0.1$ models with a normalisation constant of 5.05×10^{-21}.

Since the DM only interacts with NM through gravity, the Euler equation for the DM component does not contain any non-trivial NM-related terms except the gravitational potential Φ. Hence, the GW signature from the AIC of a DMRWD can be separated into the DM and NM contributions:

$$h_+ = h_{+,1} + h_{+,2},$$
$$h_{+,i} = \frac{3}{2} \frac{G}{Dc^4} \sin^2\theta \frac{d^2}{dt^2} I_{zz,i}. \quad (18)$$

To compute $h_{+,i}$, we can make use of Equation (16) in Ott et al. (2004), and substitute all the components of $\vec{v}$ and ρ by the corresponding DM/NM values.
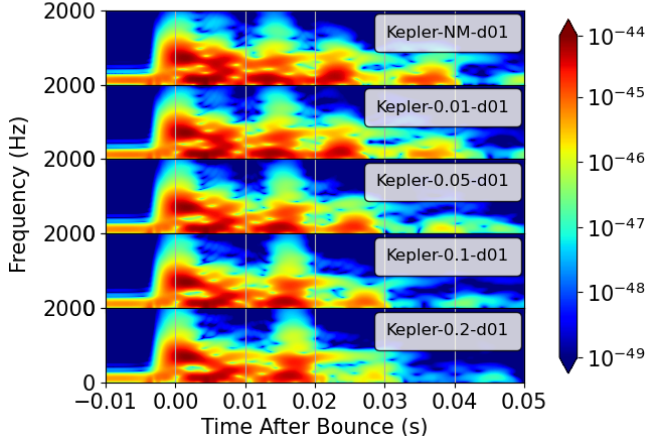
Figure 7. Power spectral density of DMAIC GWs for DM-RWDs rotating in the Kepler rule with $\alpha_d = 0.1$.

Table 2. GW mismatch (in %) with respect to the pure NM model for DMAICs with different initial rotation profiles. See Table 1 for the simulation parameters of these models.

-	Rigid	Kepler-d001	Kepler-d01
DM-0.01	0.306	13.570	19.217
DM-0.03	0.870	26.151	42.386
DM-0.05	1.263	29.103	41.173
DM-0.07	1.596	36.149	41.169
DM-0.09	1.844	38.256	44.517
DM-0.1	1.992	40.916	43.785
DM-0.2	2.784	41.845	52.794

It is also a common practice to study GW strains by the time-frequency analysis. To obtain the GW spectrogram, we perform a windowed Fourier transform:

$$\tilde{h}^*(f,t) = \int_{-\infty}^{\infty} h_+(\tau)w(t,\tau)\exp(-2\pi i f\tau)d\tau. \quad (19)$$

Here, $w(t,\tau)$ is the window function, and we choose it as the Hann window.

We first show the AIC GWs generated by the rigidly-rotating DMRWD models in Figure 5. The GWs are all generic Type I waveforms (Fryer & New 2011). There are no considerable differences in the GW signature with respect to all DM-admixed models. This is in contrast with the results presented by Zha et al. (2019b), where they show enhanced amplitudes during $\bar{t} = 0$ s. And this is because the contributions to the GW strains are mainly from the innermost core (~ 10 km). We have shown in the previous section that the effects of admix-

ing 0.1 GeV DM on the NM density profile are mainly at the NM outer envelope. The NM collapse dynamics are also generic for all DM-admixed models. We append the NM density contour plots of models NM-Rigid and DM-Rigid-0.2 in Figure 4 as reference. We observe that the dense core, which corresponds to the major part of the proto-neutron star of the DM-admixed model is almost identical to that of the pure NM counterpart. And this explains why The GW signatures from rigidly-rotating DMRWDs are all generic.

However, the situation is different for differentially rotating progenitors. We show the GW strains of the Kepler-rotating and $\alpha_d = 0.1$ model in Figure 6. We find that the admixture of DM indirectly suppresses the post-bounce 3rd and 4th peaks of the GW strains. And this could also be observed as the gradual disappearance of the 3rd and 4th spectral peaks in Figure 7. Therefore, the GW strains of DMAIC are qualitatively different from that of the pure NM model. We find that the spectral peak exists for the pure NM model because the reflected shock waves pass through the NM core and makes it pulsate non-radially. The corresponding pulsation for the DM-admixed models is smaller, resulting in a weaker GW signature. We find similar results for the Kepler-rotating and $\alpha_d = 0.01$ model, except that the 4th spectral peak never exists for the pure NM and hence, the DM-admixed models.

The DM component is more diffusive for fermionic DM with a particle mass of 0.1 GeV. As such, the collapse dynamics of the DM component could not produce GW signatures comparable to that of the NM component. The effects of DM admixture on the total GW signatures are, therefore, indirect. To quantitatively determine whether such effects could be observable, we compute the mismatch $\mathfrak{M}$, which quantifies how similar/dissimilar two waveforms are (Reisswig & Pollney 2011; Richers et al. 2017):

$$\mathfrak{M} = 1 - \max\left(\frac{\langle h_a, h_b \rangle}{\sqrt{\langle h_a, h_a \rangle \langle h_b, h_b \rangle}}\right). \quad (20)$$

The second term here contains the match between two waveforms h_a and h_b:

$$\langle h_a, h_b \rangle = \int_0^{\infty} \frac{4\tilde{h_a}^* \tilde{h_b}}{s} df. \quad (21)$$

Here, s is the estimated noise amplitude spectral density of the Advanced LIGO (Barsotti et al. 2018). $\tilde{h}^*$ is the Fourier transform of the GW strain, which is just Equation 19 but with $w(t,\tau) = 1$. The mismatch is maximized over the relative phase, amplitudes, and arrival

times. We follow Zha et al. (2019b) to set the integration limit of Equation 21 to be from 100 Hz to 2000 Hz. The computations are facilitated through the open-source package PyCBC (Nitz et al. 2022). We extract GW waveforms for all the models listed in Table 1 with a time window of $-0.01 < \bar{t} < 0.05$ s, and compute the mismatches with respect to the pure NM model. The results are listed in Table 2. The mismatches for the rigidly-rotating DMAIC models are small, which is no surprise because the GW waveforms of the DM-admixed models in such a scenario are very similar to that of the pure NM counterpart. The mismatches for the Kepler-rotating DMAIC models, however, are large. And this might be because the DM admixture significantly affects the GW frequency spectrum. The presence of a 1 % of DM can be inferred from future GW detection produced by DMAIC, if Advanced LIGO can distinguish two waveforms with an accuracy better than 14 %.

3.2. *The Compact Dark Matter Limit*

The properties of a Fermionic DM-admixed compact star were shown to be sharply changing around DM particle mass of 0.1 GeV (Leung et al. 2022). To better capture the transitional effects from a sub-GeV to GeV mass, we include progenitor models admixed with fermionic DM of particle mass 0.3 GeV. Furthermore, the progenitors are all differentially-rotating DMRWDs with $\alpha_d = 0.5$. For reference, we include the parameters of our appended models in Table 3. We generally find similar collapse dynamics for the DM and NM components as those of the diffusive DM limit. For instance, we find a delay in the NM bounce time and the successful formation of a DM-admixed neutron star. The in-depth discussion of the collapse dynamics of DMAIC under the compact DM limit would therefore be omitted.

3.2.1. *Gravitational Waves from the Dark Matter Component*

In this section, we focus on the GW signature produced by a DMAIC event. As an example, we show the GW strains of a particular model Kepler-0.05-d05 in Figure 8. The DM GW strain has amplitudes comparable to that of the NM and produces secondary oscillations on top of the NM GW strain. And this is in contrast to the diffusive DM limit. The DM component, which couples to a highly differentially rotating NM configuration set by $\alpha_d = 0.5$, become a spheroid. The vigorous non-spherical collapse dynamics thus generate a considerable magnitude of GWs. We analyze the GW strains by plotting their spectrograms in Figure 9. We find that the admixture of DM greatly suppresses the NM GW strains around the NM core bounce, which is of no surprise because the NM mass and compactness
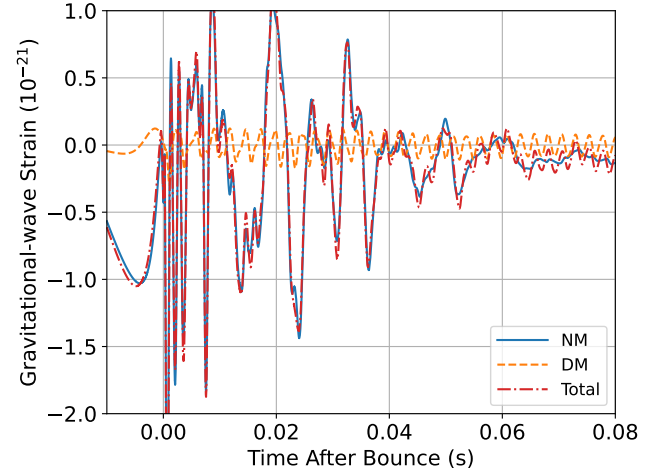

Figure 8. The magnified plot of the NM (blue solid line), DM (orange dashed line) and, total (red dashed-dotted line) GW strains for the Kepler-0.05-d05 model. Here, a distance of $D = 10$ kpc is assumed.
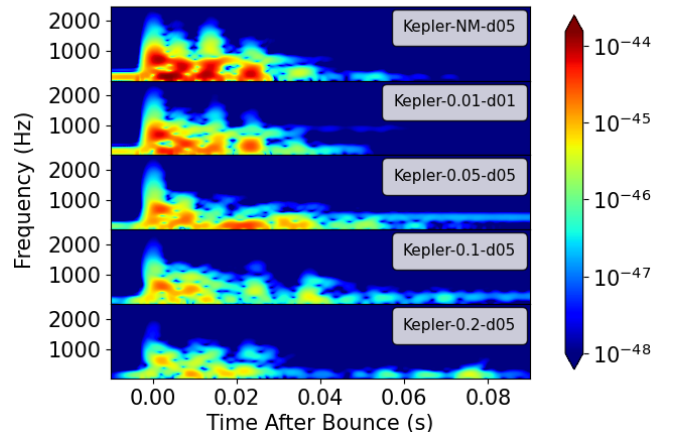

Figure 9. Same as Figure 7, but for DMRWDs rotating in the Kepler rule with $\alpha_d = 0.5$.

are reduced substantially when DM is admixed (c.f. Table 3). We also find that the DM GW strains show up as a continuous low-frequency (< 1000 Hz) signal in the spectrogram before $\bar{t} = 0.1$ s. This is important because convection-related GW signals occur after $\bar{t} = 0.1 - 0.2$ s (Zha 2019). Therefore, any low-frequency signals observed before $\bar{t} = 0.1$ s could be a direct evidence of a compact DM admixture. The DM GW waveforms (see Figure 10) are consistent with the Type III collapsing polytrope waveforms presented in Fryer & New (2011).

3.2.2. *Detection Prospect*

In the last section, we show that the DM GW signatures are strong enough to influence the total GW strains directly. What would be their detectability?

Table 3. Same as Table 1, but for differentially rotating DMAIC progenitors that have $\alpha_d = 0.5$, $\Omega_c = 45.2$ s^{-1}, and the DM particle mass of 0.3 GeV. We also append the NM compactness $\mathfrak{C} = 2GM_{\mathrm{NM}}/R_{\mathrm{eNM}}c^2$.

Model	M_{NM}	M_{DM}	$\log_{10}\rho_{1c}$	R_{eNM}	R_{eDM}	ϵ_{DM}	t_b	$\log_{10}\rho_{1b}$	$\log_{10}\rho_{2b}$	M_{PNS}	$\mathfrak{C}$
-	$(M_\odot)$	$(M_\odot)$	(gcm^{-3})	(km)	(km)	-	(ms)	(gcm^{-3})	(gcm^{-3})	$(M_\odot)$	(10^{-3})
Kepler-NM-d05	1.771	-	-	916	-	0.00	29.087	-	14.351	1.604	5.71
Kepler-0.01-d05	1.672	0.017	9.968	929	157	0.01	30.595	12.720	14.345	1.516	5.32
Kepler-0.03-d05	1.525	0.047	10.206	948	187	0.03	32.426	12.826	14.339	1.379	4.75
Kepler-0.05-d05	1.410	0.074	10.313	961	202	0.05	33.778	12.856	14.336	1.267	4.33
Kepler-0.07-d05	1.313	0.099	10.383	967	212	0.07	34.899	12.866	14.332	1.170	4.01
Kepler-0.09-d05	1.229	0.122	10.434	967	220	0.09	35.888	12.871	14.332	1.090	3.75
Kepler-0.1-d05	1.191	0.132	10.454	967	223	0.1	36.348	12.873	14.333	1.052	3.64
Kepler-0.2-d05	0.896	0.224	10.588	935	246	0.2	40.396	12.872	14.331	0.767	2.83
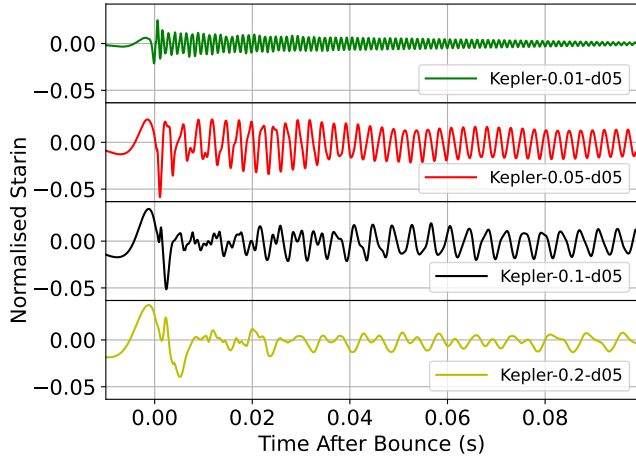
Figure 10. Same as Figure 5, but for the DM GWs of the Kepler-rotating DMAIC models with $\alpha_d = 0.5$ only. The normalisation constant is 6.07×10^{-21}.

We compute the dimensionless characteristic GW strain (Flanagan & Hughes 1998):

$$h_{\mathrm{char}} = \sqrt{\frac{2}{\pi^2}\frac{G}{c^3}\frac{1}{D^2}\frac{dE_{\mathrm{GW}}}{df}}. \quad (22)$$

Here, $\frac{dE_{\mathrm{GW}}}{df}$ is the GW spectral energy (Murphy et al. 2009):

$$\frac{dE_{\mathrm{GW}}}{df} = \frac{3}{5}\frac{G}{c^5}(2\pi f)^2|\tilde{h}_+|^2. \quad (23)$$

We compare $h_{\mathrm{char}}f^{-1/2}$ with the Advanced LIGO noise spectral density $\sqrt{s(f)}$ in Figure 11. In the same figure, we mark vertical lines corresponding to the peak frequency of the DM GW waveforms (see Figure 12). We choose the sampling window to be $\bar{t} > 0$ s. The DM characteristic GW strains corresponding to the frequency peaks are above the Advanced LIGO sensitivity
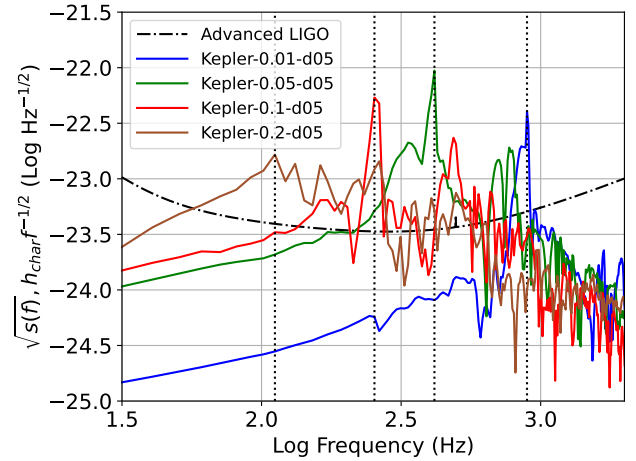

Figure 11. Scaled characteristic DM GW strains for the differentially-rotating DMAIC models with $\alpha_d = 0.5$. Peak frequencies obtained from the Fourier transform are marked as vertical black dotted lines.

curve, which is true for all of our considered models for all our considered models, assuming $D = 10$ kpc. Hence, the GW signature of a collapsing, compact DM in a Milky Way DMAIC event should be detectable by Advanced LIGO. Our results represent be the first-ever numerical calculation of the GW waveforms of a collapsing DM core in a compact star.

We discovered that the DM GW peak frequency is reduced when the DM fraction is increased. We show this trend in Figure 13. Note that in the figure, we include data points extracted from simulations with Kepler-rotating (Kepler-0.5), rapidly rigid (Rigid-Crit), and slowly rigid (Rigid-Slow) rotating progenitors. In particular, rapidly rigid rotating models have an angular velocity of 0.97 that of the critical velocity, and slowly
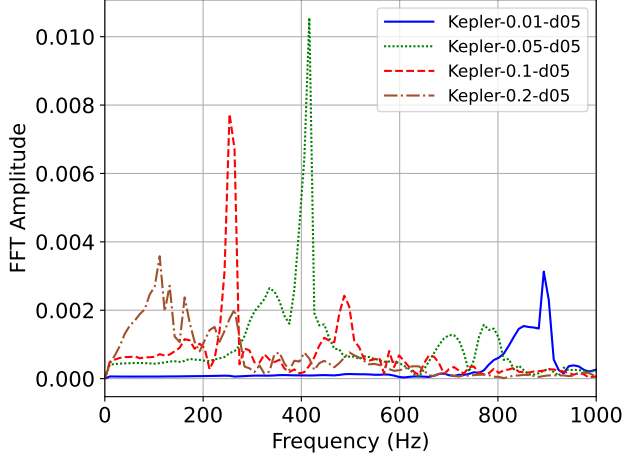
Figure 12. Fourier transformed amplitude of the DM GWs against frequency for 4 different DMAIC models with $\alpha_d = 0.5$.
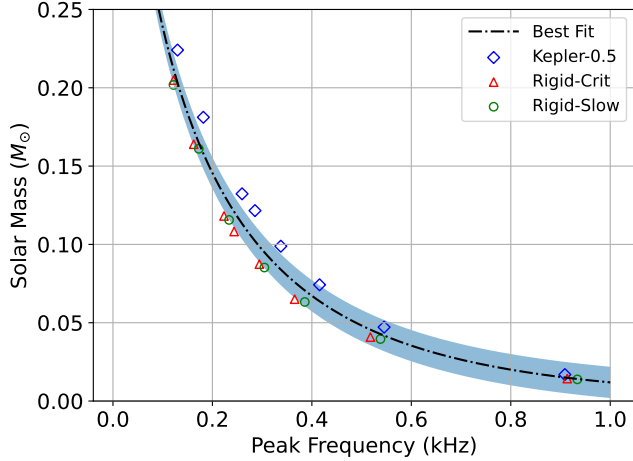

Figure 13. The DM mass against GW peak frequency for DMAIC with a DM particle mass of 0.3 GeV. Note that we include differentially (Kepler-0.5), rapidly rigid (Rigid-Crit), and slowly rigid (Rigid-Slow) rotating progenitors. The black dash-dotted line represents the best fit curve as stated in Equation 24, and the blue strip is the mean-absolute error of our fitting.

rigid rotating models have $\Omega_c = 1$ rad s^{-1}. The figure shows a relationship between the DM mass and its peak frequency. We fit the relation by:

$$M_1 = 0.572\exp(-3.873f_1^{0.646}) \qquad (24)$$

Here, M_1 is the DM mass in solar mass, and f_1 is the DM GW peak frequency in kHz. The relation is valid for $\sim 100 - 1000$ Hz. Note that we include differentially rotating, as well as rapid and slowly but rigidly rotating models in fitting this relation. Therefore, this relation should be model-independent, provided that the DM

particle mass is 0.3 GeV. From the application aspect, one can (as we proved that it is possible to) directly detect DM GWs from AIC events. Then, one can infer the DM GW peak frequency from the raw signals. Equation 24 can then be applied to directly measure the amount of DM admixture, assuming the DM particle mass to be 0.3 GeV. The exploration of such relations for higher DM particle mass would be an interesting future study. Finally, we will show the detectability of DM GWs from rigidly rotating progenitors in Appendix B.

4. CONCLUSION

We presented two-dimensional simulations of DMAIC with self-consistent modeling of the DM dynamics. Regardless of the DM particle mass and compactness, the DM component will follow the collapse of the NM component to become a bound DM core with a time scale comparable to that of the NM. This result demonstrates numerically, for the first time how a DM-admixed neutron star could form through DMAIC. We also find that the NM bounce time is delayed and the proto-neutron star mass is reduced when DM is admixed, similar as those by Leung et al. (2019) and Zha et al. (2019a), where the DM component is modeled as a fixed compact core.

Due to the weak electromagnetic signals produced by the gravitational collapse of WDs, GW becomes an important and reliable channel to detect and study AIC. We computed the GW signatures for both the NM and DM components using the quadrupole formula. For DM with a particle mass of 0.1 GeV, the DM component is more diffusive and extended. Hence, the collapse of the DM component does not produce a significant GW signal. However, the admixture of such DM indirectly influences the NM signal by suppressing the NM GW spectral peaks after the NM core bounce. The significant alteration of the NM GW frequency spectrum also makes the DMAIC waveforms easily detectable by GW detectors, which show a 14 % mismatch with the pure NM counterpart with only 1 % of DM admixed. For DM with a particle mass of 0.3 GeV, the DM component is more compact. The admixture of DM greatly reduces the NM mass and hence its compactness. The NM GW signal at bounce is therefore decreased substantially. However, the DM component is massive and compact enough to produce a GW signal comparable to that of the NM counterpart during its dynamical collapse. The DM GW adds up to the NM GW to produce secondary oscillations. These oscillations could be seen as continuous low-frequency (< 1000 Hz) signals in the GW spectrogram, occurring at $\bar{t} < 0.1$ s, which is before the

time of low-frequency GW induced by prompt convection, providing a direct evidence of the existence of DM. All the peak-frequency signals of the DM component in a Milky Way DMAIC event are detectable by the Advanced LIGO. We also discover a model-independent relationship between the DM mass and GW peak frequency, and we provide a fitting function for such a relation. The function could be used to directly measure the amount of DM admixture from the DM GW peak frequency. The function assumed the DM particle mass is 0.3 GeV and is valid for $f_1 \sim 100 - 1000$ Hz. Our result is the first-ever computations of GW from a collapsing DM core, and these findings could provide the key features to identify DM in AIC events through future GW detections.

There are possible future improvement of our calculations. First, we assumed the DM component to be non-rotating. In particular, we considered the DM to be the ideal degenerate Fermi gas. The effective quantum self-interaction allows DM to have collective motion, such as rotation. Second, we omitted detailed neutrino-transport physics in the simulations. Whether the presence of DM would significantly affect the neutrino-flavor production would be an interesting future study.. Lastly, we only include ad-hoc relativistic corrections to the gravity and dynamical equations. A more realistic picture of the collapse dynamics and the GW signature would call for solving the dynamical equations in the full general relativistic framework.

APPENDIX

A. THE FORMATION OF DARK MATTER-ADMIXED WHITE DWARF

We follow Chan et al. 2022 (submitted) to consider the progenitor of DMRWD to be a star born with an inherent admixture of DM. We assume the DM and NM to be spherically symmetric clouds having constant densities ρ_1 and ρ_2, respectively. We consider the situation with the DM radius R_1 being larger than that of the NM, R_2. The total energy E is:

$$E = -(\frac{3}{5}\frac{GM_1^2}{R_1} + \frac{3}{5}\frac{GM_2^2}{R_2} + \frac{3}{2}\frac{GM_1M_2}{R_1} - \frac{3}{10}\frac{GM_1^2R_1^2}{R_1^3}) + \frac{3}{2}NkT + \frac{1}{2}M_1v_1^2. \quad (A1)$$

Here, v_1 is the DM "thermal" velocity, $N = M_2/m_H$ is the total number of NM nuclei, and m_H is the molecular mass of hydrogen. Furthermore, we assume an extreme case of $M_1 \sim 0.1\ M_\odot$, $M_2 \sim 10.0\ M_\odot$. For a typical collapsing molecular cloud, we have $T \sim 150$ K and $\rho_2 \sim 10^8 m_H$ cm^{-3}, and hence $R_2 = 3.05 \times 10^{16}$ cm is smaller than the Jeans radius. We solve $E(R_2) = 0$ to obtain the maximum DM velocity of DM $v_{1max} \sim 1.27 \times 10^6$ cm s^{-1}. Any $v_1 < v_{1max}$ would give us a set of solution for R_1 and ρ_1. However, the most probable DM speed (assuming a Maxwell distribution) is $v_{p1} \sim 10^7$ cm s^{-1}. To take the velocity of DM into account, the bounded DM fraction is given by f:

$$f = \frac{\int_0^{u_1} u^2 \exp(-u^2)du}{\int_0^\infty u^2 \exp(-u^2)du}. \quad (A2)$$

Here, $u = v/v_{p1}$, and $u_1 = v_1/v_{p1}$. We take a particular $v_1 = 1.23 \times 10^6$ cm s^{-1}, and give two sets of solutions in (R_1, ρ_1) for $E < 0$: $(1.71 \times 10^{18}$ cm, 3860 GeV/cm^3) and $(6.10 \times 10^{16}$ cm, 8.48×10^7 GeV/cm^3). The required DM density in the first set of solutions is based on the state-of-the-art simulations, which showed that the DM density at the galactic bulge could be ~ 3600 GeV cm^{-3} (Piffl et al. 2014). The required DM density in the other set of solutions is much larger. However, such a value is possible near the galactic center, and values with a similar order of magnitude have been adopted in studying the effect of DM annihilation on main-sequence stars (Moskalenko & Wai 2006; Iocco 2008). In conclusion, our estimations considering the DM velocity dispersions show that it is possible to trap a DM of 0.1 $M_\odot$ during the star-forming phase, provided that the molecular cloud is in the vicinity of the galactic center. There might be concern about whether the DM would follow the collapse of the NM to form a composite bound object. We show in the earlier section that a collapsing NM component would eventually induce a collapsing DM component to form a DM-admixed stellar object. And this would, in our case, be a DM-admixed neutron star. Also, the collapse of the DM component happens
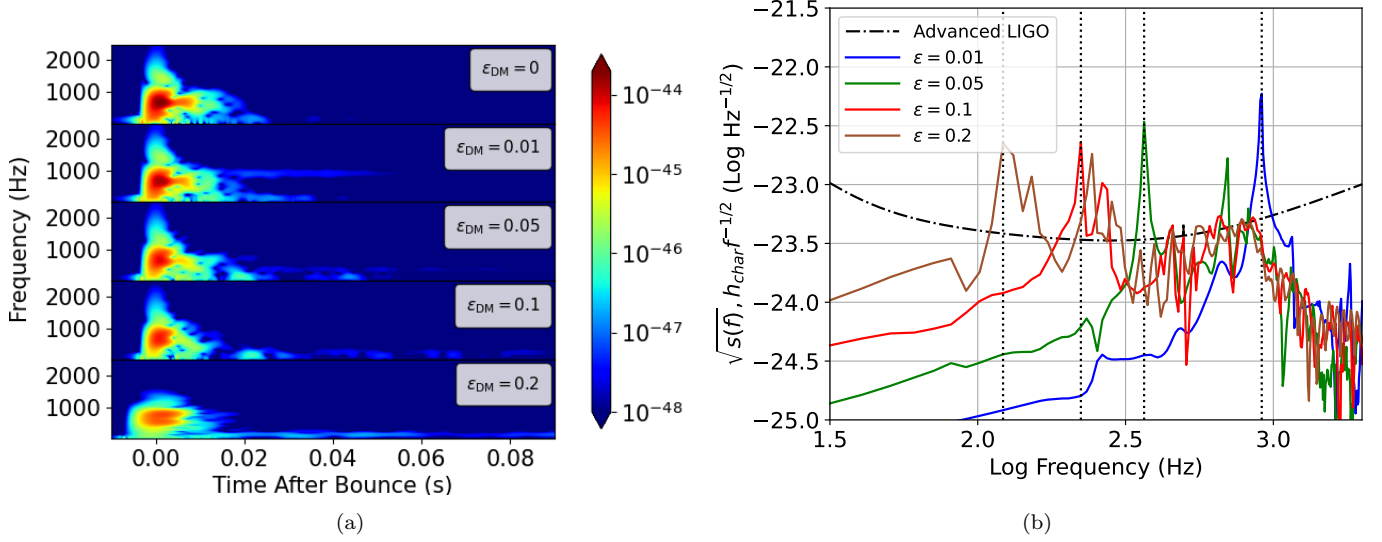
Figure 14. (a) Power spectral density of DMAIC GWs for rigidly-rotating progenitors with increasing DM mass fraction ϵ_{DM}. (b) Same as Figure 11, but for characteristic wave strains of models presented in (a) and their comparison with the Advanced LIGO sensitivity curve.

with a time scale comparable to that of the NM, regardless of its size and mass. By simple scaling relations, we can roughly conclude that the same scenario should also hold for molecular cloud collapse. Therefore, a zero-age main-sequence with an inherent DM admixture should be possible, though a detailed numerical simulation shall be employed to justify our conjecture.

B. DARK MATTER GRAVITATIONAL WAVES FOR RIGIDLY-ROTATING PROGENITORS

In section 3.2.2 we showed the features for DM GWs from differentially-rotating progenitors and proved that they are detectable by the Advanced LIGO, provided that the DM particle mass is 0.3 GeV. Here, we perform a similar analysis for rigidly-rotating progenitors. In Figure 14 (a), we show the GW spectrograms for rigidly-rotating progenitors. These progenitors are rotating at ~ 0.97 that of the critical velocity and have increasing DM mass fraction ϵ_{DM} from 0 to 0.2. We observe that the DM GWs can also be captured as continuous low-frequency (< 1000 Hz) signals. In Figure 14 (b), we observe that all peak frequency signals of the DM GWs are detectable by the Advanced LIGO.

REFERENCES

Abbott, R., et al. 2020, The Astrophysical Journal, 896, L44, doi: 10.3847/2041-8213/ab960f

Abdikamalov, E. B., Ott, C. D., Rezzolla, L., et al. 2010, Phys. Rev. D, 81, 044012, doi: 10.1103/PhysRevD.81.044012

Aksenov, A. G., & Blinnikov, S. I. 1994, A&A, 290, 674

Arun, K., Gudennavar, S. B., Prasad, A., & Sivaram, C. 2019, Ap&SS, 364, 24, doi: 10.1007/s10509-019-3511-6

Barsotti, L., Fritschel, P., Evans, M., & Gras, S. 2018, LIGO-T1800042-v5, Tech. rep., LIGO

Bell, N. F., Melatos, A., & Petraki, K. 2013, Phys. Rev. D, 87, 123507, doi: 10.1103/PhysRevD.87.123507

Bera, P., & Bhattacharya, D. 2016, Monthly Notices of the Royal Astronomical Society, 456, 3375, doi: 10.1093/mnras/stv2823

Bhat, S. A., & Paul, A. 2020, European Physical Journal C, 80, 544, doi: 10.1140/epjc/s10052-020-8072-x

Boshkayev, K. 2018, Astronomy reports, 62, 847

Bramante, J., Fukushima, K., & Kumar, J. 2013, Phys. Rev. D, 87, 055012, doi: 10.1103/PhysRevD.87.055012

Brooks, J., Schwab, J., Bildsten, L., Quataert, E., & Paxton, B. 2017, The Astrophysical Journal, 843, 151, doi: 10.3847/1538-4357/aa79a6

Chan, H.-S., chung Chu, M., Leung, S.-C., & Lin, L.-M.
2021, The Astrophysical Journal, 914, 138,
doi: 10.3847/1538-4357/abfd32

Chatterjee, D., Fantina, A. F., Chamel, N., Novak, J., &
Oertel, M. 2017, Monthly Notices of the Royal
Astronomical Society, 469, 95, doi: 10.1093/mnras/stx781

Clea, S., Kenath, A., Sivaram, C., & Gudennavar, S. 2020,
Physics of the Dark Universe, 30, 100727,
doi: https://doi.org/10.1016/j.dark.2020.100727

Colella, P., & Woodward, P. R. 1984, Journal of
Computational Physics, 54, 174,
doi: 10.1016/0021-9991(84)90143-8

Couch, S. M., Graziani, C., & Flocke, N. 2013, The
Astrophysical Journal, 778, 181,
doi: 10.1088/0004-637x/778/2/181

Dar, A., Kozlovsky, B. Z., Nussinov, S., & Ramaty, R.
1992, ApJ, 388, 164, doi: 10.1086/171138

Darbha, S., Metzger, B. D., Quataert, E., et al. 2010,
MNRAS, 409, 846, doi: 10.1111/j.1365-2966.2010.17353.x

Das, H. C., Kumar, A., & Patra, S. K. 2021, PhRvD, 104,
063028, doi: 10.1103/PhysRevD.104.063028

Davis, M., Efstathiou, G., Frenk, C. S., & White, S. D. M.
1985, ApJ, 292, 371, doi: 10.1086/163168

Dessart, L., Burrows, A., Ott, C. D., et al. 2006, The
Astrophysical Journal, 644, 1063, doi: 10.1086/503626

Eriguchi, Y., & Mueller, E. 1985, A&A, 146, 260

Fink, M., Kromer, M., Hillebrandt, W., et al. 2018, A&A,
618, A124, doi: 10.1051/0004-6361/201833475

Finn, L. S., & Evans, C. R. 1990, ApJ, 351, 588,
doi: 10.1086/168497

Flanagan, E. E., & Hughes, S. A. 1998, Phys. Rev. D, 57,
4535, doi: 10.1103/PhysRevD.57.4535

Franzon, B., & Schramm, S. 2015, Phys. Rev. D, 92,
083006, doi: 10.1103/PhysRevD.92.083006

Fryer, C. L., & New, K. C. B. 2011, Living Reviews in
Relativity, 14, 1, doi: 10.12942/lrr-2011-1

Gottlieb, S., Ketcheson, D., & Shu, C.-W. 2011, Strong
Stability Preserving Runge-Kutta and Multistep Time
Discretizations (WORLD SCIENTIFIC),
doi: 10.1142/7498

Gvaramadze, V. V., Gräfener, G., Langer, N., et al. 2019,
Nature (London), 569, 684

Hachisu, I. 1986, ApJS, 61, 479, doi: 10.1086/191121

Iocco, F. 2008, ApJL, 677, L1, doi: 10.1086/587959

Kawaler, S. D. 2004, in Stellar Rotation, ed. A. Maeder &
P. Eenens, Vol. 215, 561

Langer, N., Yoon, S. C., Petrovic, J., & Heger, A. 2003,
arXiv e-prints, astro.
https://arxiv.org/abs/astro-ph/0302232

Lee, B. K. K., Chu, M.-c., & Lin, L.-M. 2021, ApJ, 922,
242, doi: 10.3847/1538-4357/ac2735

Leung, K.-L., Chu, M.-c., & Lin, L.-M. 2022, Phys. Rev. D,
105, 123010, doi: 10.1103/PhysRevD.105.123010

Leung, S.-C., & Nomoto, K. 2019, PASA, 36, e006,
doi: 10.1017/pasa.2018.49

Leung, S.-C., Nomoto, K., & Suzuki, T. 2020, The
Astrophysical Journal, 889, 34,
doi: 10.3847/1538-4357/ab5d2f

Leung, S.-C., Zha, S., Chu, M.-C., Lin, L.-M., & Nomoto,
K. 2019, The Astrophysical Journal, 884, 9,
doi: 10.3847/1538-4357/ab3b5e

Liebendorfer, M. 2005, The Astrophysical Journal, 633,
1042–1051, doi: 10.1086/466517

Liu, D., & Wang, B. 2020, Monthly Notices of the Royal
Astronomical Society, 494, 3422,
doi: 10.1093/mnras/staa963

Lopes, J., & Lopes, I. 2019, The Astrophysical Journal,
879, 50, doi: 10.3847/1538-4357/ab2392

Margalit, B., Berger, E., & Metzger, B. D. 2019, ApJ, 886,
110, doi: 10.3847/1538-4357/ab4c31

Mignone, A. 2014, Journal of Computational Physics, 270,
doi: 10.1016/j.jcp.2014.04.001

Moenchmeyer, R., Schaefer, G., Mueller, E., & Kates, R. E.
1991, A&A, 246, 417

Moriya, T. J. 2016, ApJL, 830, L38,
doi: 10.3847/2041-8205/830/2/L38

Moskalenko, I. V., & Wai, L. L. 2006, arXiv e-prints, astro.
https://arxiv.org/abs/astro-ph/0608535

Müller, B., Dimmelmeier, H., & Müller, E. 2008, A&A, 489,
301, doi: 10.1051/0004-6361:200809609

Murphy, J. W., Ott, C. D., & Burrows, A. 2009, ApJ, 707,
1173, doi: 10.1088/0004-637X/707/2/1173

Narain, G., Schaffner-Bielich, J., & Mishustin, I. N. 2006,
Phys. Rev. D, 74, 063003,
doi: 10.1103/PhysRevD.74.063003

Nitz, A., Harry, I., Brown, D., et al. 2022, gwastro/pycbc:
v2.0.5 release of PyCBC, v2.0.5, Zenodo,
doi: 10.5281/zenodo.6912865

Nomoto, K., & Kondo, Y. 1991, ApJL, 367, L19,
doi: 10.1086/185922

Ott, C. D. 2009, Classical and Quantum Gravity, 26,
063001, doi: 10.1088/0264-9381/26/6/063001

Ott, C. D., Burrows, A., Livne, E., & Walder, R. 2004,
ApJ, 600, 834, doi: 10.1086/379822

Ott, C. D., Ou, S., Tohline, J. E., & Burrows, A. 2005,
ApJL, 625, L119, doi: 10.1086/431305

Pfannes, J. M. M., Niemeyer, J. C., & Schmidt, W. 2010,
A&A, 509, A75, doi: 10.1051/0004-6361/200912033

Piffl, T., Binney, J., McMillan, P. J., et al. 2014, MNRAS, 445, 3133, doi: 10.1093/mnras/stu1948

Pshirkov, M. S., Dodin, A. V., Belinski, A. A., et al. 2020, Monthly Notices of the Royal Astronomical Society: Letters, 499, L21, doi: 10.1093/mnrasl/slaa149

Raen, T. J., Martínez-Rodríguez, H., Hurst, T. J., et al. 2021, Monthly Notices of the Royal Astronomical Society, 503, 5611, doi: 10.1093/mnras/stab865

Reisswig, C., & Pollney, D. 2011, Classical and Quantum Gravity, 28, 195015, doi: 10.1088/0264-9381/28/19/195015

Richers, S., Ott, C. D., Abdikamalov, E., O'Connor, E., & Sullivan, C. 2017, PhRvD, 95, 063019, doi: 10.1103/PhysRevD.95.063019

Ruiter, A. J., Ferrario, L., Belczynski, K., et al. 2019, Monthly Notices of the Royal Astronomical Society, 484, 698, doi: 10.1093/mnras/stz001

Shen, H., Toki, H., Oyamatsu, K., & Sumiyoshi, K. 2011, ApJS, 197, 20, doi: 10.1088/0067-0049/197/2/20

Skinner, M. A., Burrows, A., & Dolence, J. C. 2016, ApJ, 831, 81, doi: 10.3847/0004-637X/831/1/81

Spruit, H. C. 1998, A&A, 333, 603. https://arxiv.org/abs/astro-ph/9802141

Sulistiyowati, Wulandari, H., Dermawan, B., Arifyanto, M. I., & Ibrahim, I. 2014, in American Institute of Physics Conference Series, Vol. 1589, 4th International Conference on Mathematics and Natural Sciences (ICMNS 2012): Science for Health, Food and Sustainable Energy, 33–36, doi: 10.1063/1.4868744

Toro, E. 2009, Riemann Solvers and Numerical Methods for Fluid Dynamics: A Practical Introduction, doi: 10.1007/b79761

Wang, B. 2018, Monthly Notices of the Royal Astronomical Society, 481, 439, doi: 10.1093/mnras/sty2278

Wang, B., Justham, S., Liu, Z.-W., et al. 2014, Monthly Notices of the Royal Astronomical Society, 445, 2340, doi: 10.1093/mnras/stu1891

Wang, B., & Liu, D. 2020, Research in Astronomy and Astrophysics, 20, 135, doi: 10.1088/1674-4527/20/9/135

Wang, B., Liu, D., & Chen, H. 2022, MNRAS, 510, 6011, doi: 10.1093/mnras/stac114

Wu, C.-Y., & Wang, B. 2018, Research in Astronomy and Astrophysics, 18, 036, doi: 10.1088/1674-4527/18/3/36

Yoon, S.-C., & Langer, N. 2004, Astronomy & Astrophysics, 419, 623–644, doi: 10.1051/0004-6361:20035822

Yoon, S.-C., & Langer, N. 2005, A&A, 435, 967, doi: 10.1051/0004-6361:20042542

Yoshida, S. 2019, Monthly Notices of the Royal Astronomical Society, 486, 2982–2994, doi: 10.1093/mnras/stz1030

Zha, S., Chu, M.-C., Leung, S.-C., & Lin, L.-M. 2019a, The Astrophysical Journal, 883, 13, doi: 10.3847/1538-4357/ab3640

Zha, S., Leung, S.-C., Suzuki, T., & Nomoto, K. 2019b, The Astrophysical Journal, 886, 22, doi: 10.3847/1538-4357/ab4b4b

Zha, S., O'Connor, E. P., Chu, M.-c., Lin, L.-M., & Couch, S. M. 2020, PhRvL, 125, 051102, doi: 10.1103/PhysRevLett.125.051102

Zingale, M., Almgren, A. S., Barrios Sazo, M., et al. 2020, in Journal of Physics Conference Series, Vol. 1623, Journal of Physics Conference Series, 012021, doi: 10.1088/1742-6596/1623/1/012021